HOMOLOGOUS EXTREME ULTRAVIOLET WAVES IN THE EMERGING FLUX REGION OBSERVED BY THE *SOLAR DYNAMICS OBSERVATORY*

Ruisheng Zheng, Yunchun Jiang, Jiayan Yang, Yi Bi, Junchao Hong, B. Yang, and Dan Yang
National Astronomical Observatories/Yunnan Observatory, Chinese Academy of Sciences, Kunming 650011, China; zhrsh@ynao.ac.cn

ABSTRACT

Taking advantage of the high temporal and spatial resolution of the *Solar Dynamics Observatory (SDO)* observations, we present four homologous extreme ultraviolet (EUV) waves within 3 hr on 2010 November 11. All EUV waves emanated from the same emerging flux region (EFR), propagated in the same direction, and were accompanied by surges, weak flares, and faint coronal mass ejections (CMEs). The waves had the basically same appearance in all EUV wavebands of the Atmospheric Imaging Assembly on *SDO*. The waves propagated at constant velocities in the range of 280–500 km s^{-1}, with little angular dependence, which indicated that the homologous waves could be likely interpreted as fast-mode waves. The waves are supposed to likely involve more than one driving mechanism, and it was most probable that the waves were driven by the surges, due to their close timing and location relations. We also propose that the homologous waves were intimately associated with the continuous emergence and cancellation of magnetic flux in the EFR, which could supply sufficient energy and trigger the onsets of the waves.

Key words: Sun: activity – Sun: corona – Sun: coronal mass ejections (CMEs)

Online-only material: animations, color figures

1. INTRODUCTION

Extreme ultraviolet (EUV) waves are well known as large-scale coronal transients with a diffuse rim of enhanced emission, expanding outward from flaring and eruptive active regions (ARs). They were first observed by the EUV Imaging Telescope (EIT) on board the *Solar and Heliospheric Observatory* (*SOHO*) spacecraft (e.g., Moses et al. 1997; Thompson et al. 1998), and hence were originally termed "EIT waves." The speed of EUV waves is in the range of 100–700 km s^{-1}, which is sometime below the coronal fast-mode speed.

In the last 14 years, though hundreds of EUV waves were researched with various observations, their nature is still strongly debated. Continuous quantitative studies and more detailed observations have led to some models being put forward. EUV waves have been initially interpreted as coronal fast-mode magnetohydrodynamic (MHD) waves triggered by associated coronal mass ejections (CMEs) or flares (e.g., Thompson et al. 1999; Wang 2000; Wu et al. 2001; Ofman & Thompson 2002; Long et al. 2008; Gopalswamy et al. 2009; Veronig et al. 2010). The model was originally considered by Uchida (1968), who suggested that chromospheric Moreton waves (Moreton 1960) were the counterparts of fast-mode coronal waves. The model can explain several characteristics of EUV waves, such as pulse broadening and amplitude drop-offs (Wills-Davey 2006; Warmuth 2010; Veronig et al. 2010), weak dependence on magnetic field direction (Thompson et al. 1998), reflection and refraction around regions with higher Alfvén speed (Thompson et al. 1999; Thompson & Myers 2009; Gopalswamy et al. 2009), constant velocity (e.g., Kienreich et al. 2009; Ma et al. 2009; Liu et al. 2010), and deceleration in the propagation (Veronig et al. 2008, 2010; Long et al. 2008). The major alternative models claim that EUV waves are not waves at all, but rather signatures of large-scale coronal restructuring during CMEs' lift-off, referred to as pseudo-waves. One proposition for pseudo-waves is the disk projection of large-scale current shells

enveloping the eruptive flux rope of associated CMEs (Delannée et al. 2008). Another suggestion is successive reconnections between expanding CMEs and the favorably oriented surrounding magnetic field (Attrill et al. 2007). Moreover, Chen et al. (2002, 2005) developed the field-line stretching model. Recently, hybrid models were proposed that included both wave and pseudo-wave scenarios (Zhukov & Auchère 2004; Cohen et al. 2009; Liu et al. 2010; Downs et al. 2011). In addition, EUV waves are also regarded as slow-mode or soliton-like waves (Wills-Davey et al. 2007; Wang et al. 2009). For details of observations and models, please refer to recent reviews (Wills-Davey & Attrill 2009; Gallagher & Long 2011; Warmuth 2010).

As to the possible generation mechanisms of EUV waves, previous studies are mainly focused on their associations with flares and CMEs (Biesecker et al. 2002; Cliver et al. 2005). Flares could trigger a freely propagating blast wave by the pressure pulse; CMEs could generate a piston-driven shock or an only initially driven shock that continues to propagate freely (Gilbert & Holzer 2004). Biesecker et al. (2002) confirmed that EUV waves were strongly associated with CMEs rather than flares. Chen (2006) found that none of the flares in the sample were associated with EUV waves, and EUV waves and expanding dimmings appeared only when CMEs were present. Cliver et al. (2005) found that nearly half of the large-scale EUV waves were associated with small flares having soft X-ray intensities below C-class. Figuring in an arbitrary minimum level of X-ray emission, Delannée (2009) suggested that each EUV wave was related to a flare. In addition, small-scale ejecta (e.g., spray surges, erupting plasmoids) could generate an initially driven shock, which travels freely after the ejection stops (Klein et al. 1999; Klassen et al. 2003).

Multiple waves are fascinating and have been studied in some cases. Gilbert & Holzer (2004) found multiple waves observed in chromospheric He I images, which involved more than one driving mechanism. Narukage et al. (2008) discovered three successive Moreton waves generated by a single flare in Hα
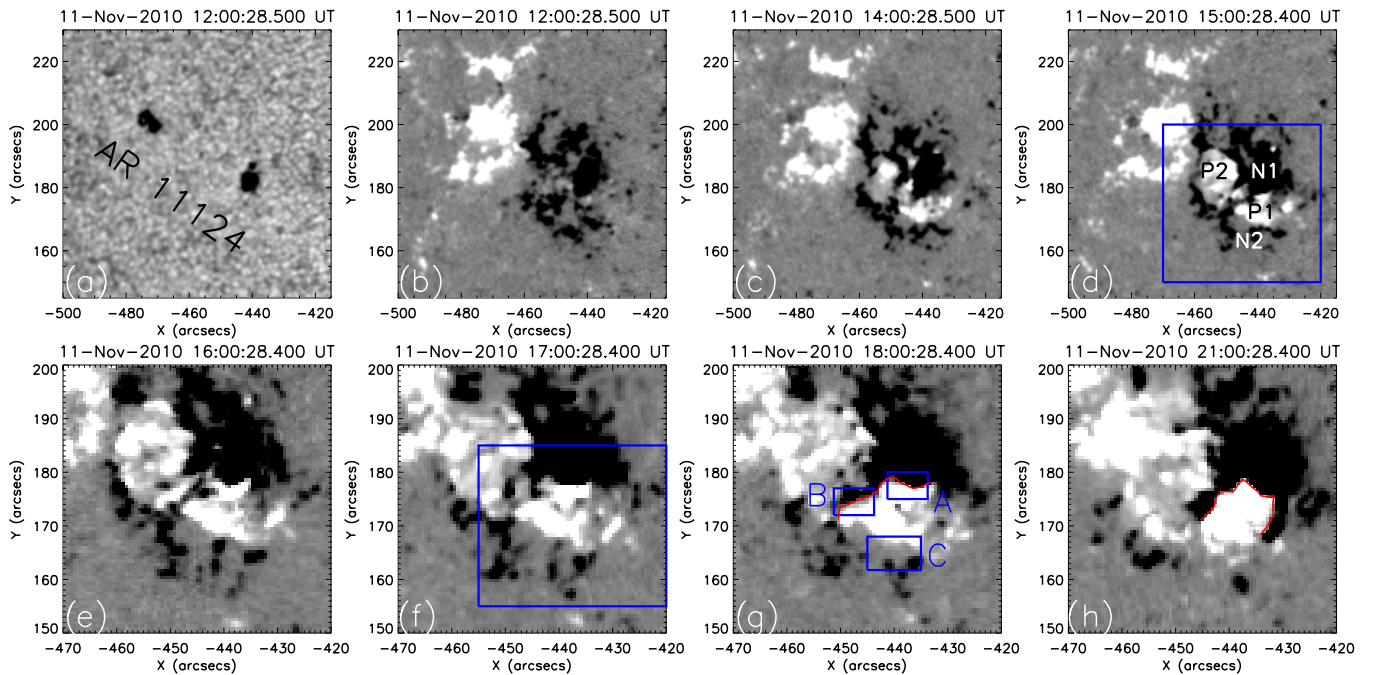
Figure 1. General appearance of NOAA AR 11124 in an HMI intensity map (panel a) and HMI magnetograms (panels b–d). The main magnetic polarities are named as P1, P2, N1, and N2. The close-up of the EFR is shown in bottom panels, whose field of view (FOV) is indicated by the box in panel d. The box in panel f denotes the main part of the EFR, and boxes of A–C in panel g show the magnetic flux cancellation regions around the PIL, marked by the red curved lines.

(A color version of this figure is available in the online journal.)

data, in which the wave origin was closely associated with a filament eruption. As to the homologous EUV waves, they were first proposed and studied in Kienreich et al. (2011), in which the waves were observed by the Extreme Ultraviolet Imager (EUVI) within 8 hr.

For understanding the nature and origin of EUV waves, it is key to get the important information on coronal conditions or the initiation and early expansion of the CME, which need high temporal and spacial observations. Since the launch of the *Solar Dynamics Observatory* (*SDO*), its high-cadence and sensitivity observations make it possible to study EUV waves in detail, and some new results have been presented (e.g., Chen & Wu 2011; Ma et al. 2011; Liu et al. 2011). In this paper, taking advantage of the *SDO* data combined with the observations from EUVI (Howard et al. 2008) on board the twin spacecrafts of *Solar-Terrestrial Relations Observatory* (*STEREO*; Kaiser et al. 2008), we concentrate on four homologous EUV waves originated from the same source region on 2010 November 11.

2. OBSERVATIONS AND DATA ANALYSIS

The four successive eruptions occurred in the same source region of NOAA AR 11124 from about 18:10 to 21:00 UT, which are labeled as E1, E2, E3, and E4. The eruptions include successive flares, CMEs, surges, and four homologous EUV waves.

We mainly use the EUV observations of the Atmospheric Imaging Assembly (AIA; Lemen et al. 2011) on *SDO*, covering a wide range of temperatures. The cadence is up to 12 s, and the pixel resolution is 0″.6. The waves and surges are visible in all AIA EUV wavelengths. We use the base difference images in 193 Å to show the wave evolution on disk. Because the background was changing for the duration, the base images for four waves were chosen before each eruption, at 18:00:07, 18:45:07, 19:30:07, and 20:40:07 UT, respectively. In order to

analyze the dynamics of the waves, we employ a time-slice approach, in which the slices start from the identified eruption center ($x = -440''$, $y = 180''$) and had a length of 500″. The running difference images may "distort the picture of large-scale disturbances caused by a CME" (Chertok & Grechnev 2005), and "real intensity decreases (coronal dimmings) and increase (such as the bright front of a coronal wave) can only be confidently identified and studied using base difference images" (Attrill 2010). So we only use the base difference images, which obtained by subtracting the base image from present image in each wavelength. The base images for time-slice approach are the first image at 18:00 UT, which could truly reveal the intensity change under the same background.

In addition, magnetograms and intensity maps from the Helioseismic and Magnetic Imager (HMI), another instrument on board *SDO*, are chosen to check the magnetic field evolution of the eruption region. The observations from the EUVI Ahead (-A) are utilized to study the evolution of the eruptions in the low corona.

3. RESULTS

3.1. Continuous Emergence and Cancellation of Magnetic Flux

The general appearance of AR 11124 is shown by an intensity map and magnetograms of HMI in Figure 1. AR 11124 had the typical simple β-type magnetic morphology (panels a and b), which consisted of a negative-polarity leading and a positive-polarity following sunspot. There was nearly no positive flux in the leading sunspot before about 12:00 UT on November 11. After that an emerging flux region (EFR) began to appear in the leading sunspot (the box in panel d), and the close-up of the EFR was shown in panels e–h. In the EFR, the new positive flux (P1 and P2) grew out of nothing in some hours and became very obvious. The new negative flux was difficultly distinguished and possibly melted into the background negative
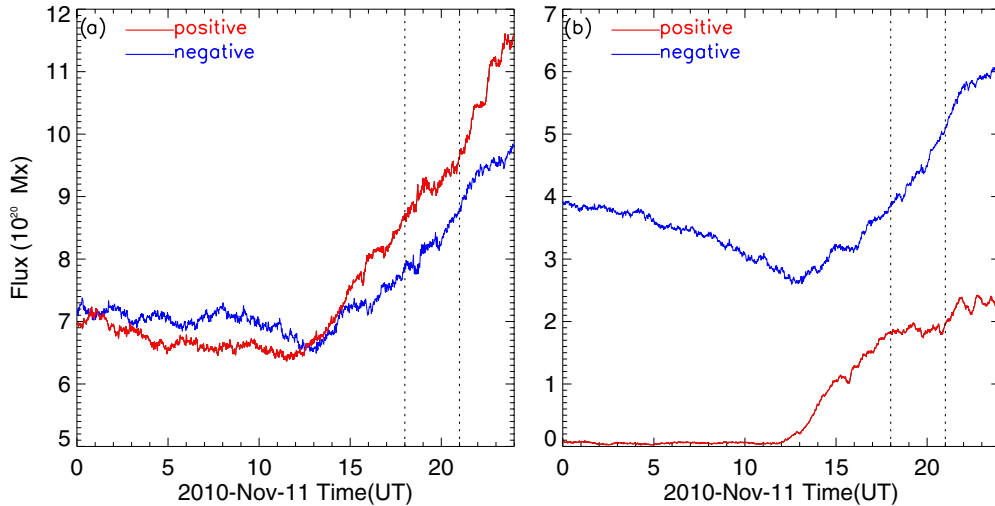
Figure 2. Changes of the positive (red) and negative (blue) magnetic fluxes for the whole AR (panel a) and for the box region in Figure 1(f) (panel b). The vertical dotted lines mark the period of the event.

(A color version of this figure is available in the online journal.)

flux (BN). Due to the continuous emergence, BN was divided into two parts (N1 and N2) and constantly collided with P1 and P2. As time went on, N2 was smaller and smaller, and nearly disappeared. Oppositely, N1 was stronger, suggestive of the new negative flux. Particularly, the polarity inversion line (PIL) in the EFR (red curves in panels g–h) changed its shape rapidly and formed a strongly curved profile, which likely resulted from the continuous emergence, cancellation, and/or convergence movement of the magnetic fluxes. A–C in panel g indicated the cancellation regions associated with the eruptions. A and B were around the PIL between P1 and N1, and C was between P1 and N2. The bottom panels show that the morphology of the magnetic field changes rapidly. Besides the emergence and cancellation, the movement of the magnetic field is also very clear. In addition, the projection effect would influence the morphology of the magnetic field. In boxes A or B, the cancellation is not obvious. However, the cancellation could be clearly identified in box C.

Figure 2 plots the changes of the magnetic fluxes for the whole AR in Figure 1(b) (panel a) and the main part of the EFR in the box region of Figure 1(f) (panel b), in which the vertical lines marked the duration of the event. The flux emergence was very obvious and continuous until the end of the day. The positive flux increased from about 12:00 UT, and the increment of the negative flux started at about 13:00 UT. The plots prior to the new fluxes emergence show a tendency to decline with weak fluctuations for both polarities fluxes, which implied that the AR was in decay. In the whole AR, the positive and negative fluxes increased about 5.2×10^{20} Mx and 3.3×10^{20} Mx, respectively. In the main EFR, the positive flux increased about 2.3×10^{20} Mx from about zero, which was consistent with the fact that the new positive flux was introduced into the preexisting negative field. The increment of the negative flux was about 3.6×10^{20} Mx, more than that of the whole AR. In panel b, it was interesting that the positive flux stopped increasing during the event and began to increase again after the eruptions, while the negative flux kept increasing sharply. It is possible that the fast growth of the negative flux initiated the encounter and cancellation between the opposite fluxes, which canceled the slow growth of the positive flux. We suggest that there is a close relation between

the eruptions and the continuous emergence and cancellation of the magnetic flux in the EFR.

3.2. Successive Eruptions

Figure 3 shows E1 (top panels) and E2 (bottom panels) in HMI magnetograms, original images of AIA 304 Å, and base difference images of AIA 193 Å. E1 was accompanied by a flare and a curved surge with a length of about 50 Mm (arrows in panels b–c), which suggested that the surge moved along the loops. The surge was rooted in A (triangles in panels a–b). Ahead of the surge, an EUV wave front appeared, followed by dimmings (panel d). E2 was also associated with a flare, a surge, an EUV wave, and dimmings. The surge was short (white arrows in panels f–g) and emanated from B (triangles in panels e–f). The wave was stronger than the first one. In addition, E2 was associated with a mini-filament eruption. The filament inserted in the interior of P1 (black arrows in panels e–f) with a typical length of about $20''$ (Wang et al. 2000; Zheng et al. 2011). The mini-filament formed during the interaction of P1 and N1, and its eruption was likely triggered by the magnetic flux cancellation.

Figure 4 displays E3 in HMI magnetograms, both original and base difference images of AIA 193 Å, which occurred in the area marked by C (triangles in panels a–b). Before E3's onset, some dark mass flowed from C, which was probably the precursor of the surge (the white arrow in panel b). The surge was spectacular and reached a maximum length of about 200 Mm (white arrows in panels c–d). As a result, the ambient coronal loops disappeared (the black arrow in panel b), leaving dimmings behind. The EUV wave in E3 was strongest, and its evolution is shown in the bottom panels. It dominated in the southeast and had a semicircle bright front, followed by faint dimmings. It was different from the deep dimmings around the eruption center, which represented the mass evacuation.

Similar to Figure 4, Figure 5 shows E4, which also is associated with a flare and a surge from C (triangles in panels a–b). Dark mass flow also appeared before the E4 occurrence, as the precursor of the surge (the white arrow in panel b). Several minutes later, the overlying loops also erupted (black arrows in
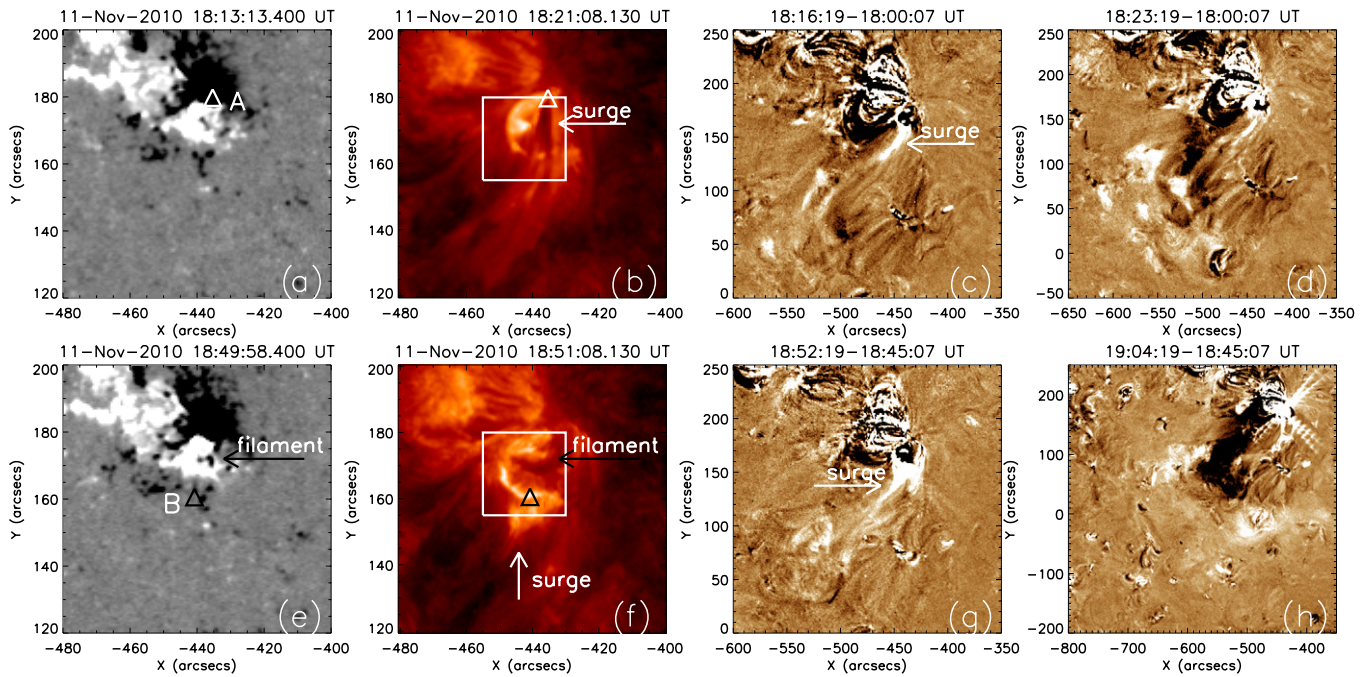
Figure 3. Evolutions of E1 (upper panels) and E2 (bottom panels), shown in HMI magnetograms, original images in AIA 304 Å, and base difference images in AIA 193 Å. The triangles indicate the eruption locations in A and B. The white (black) arrows indicate the surges (filament). The box region is chosen to calculate the light curves of the eruptions.

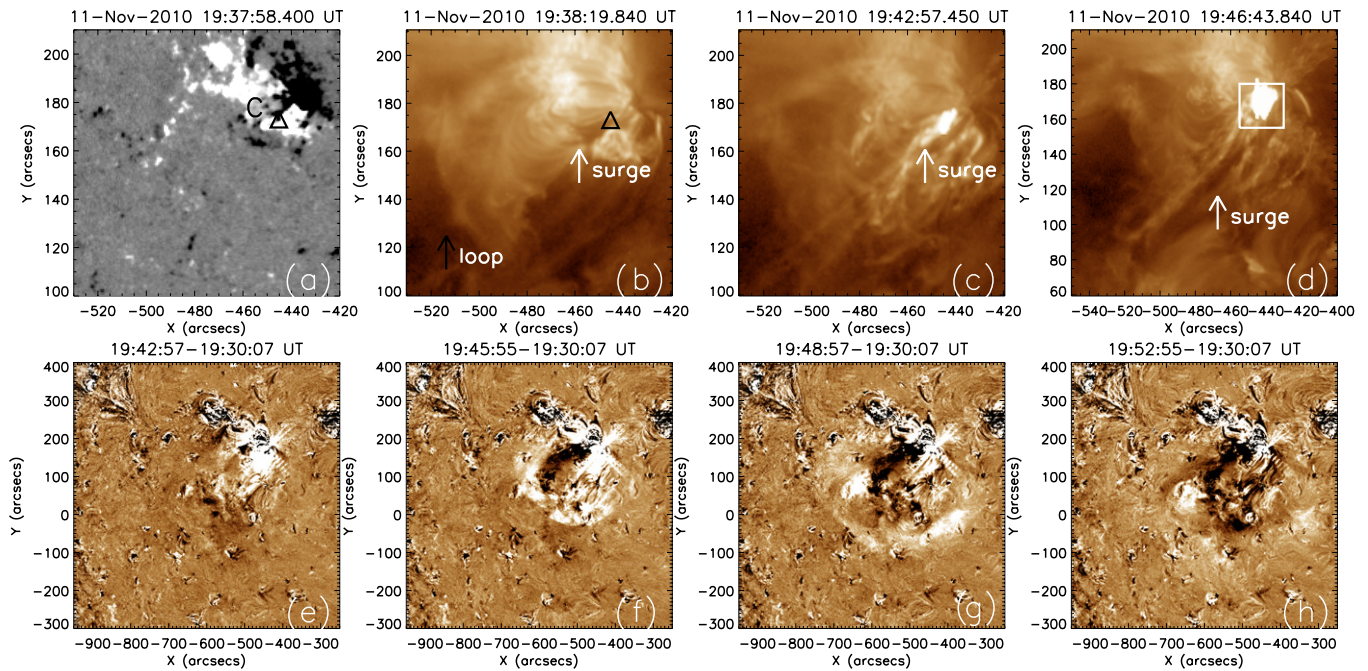(A color version of this figure is available in the online journal.)

Figure 4. Evolution of E3, shown in the HMI magnetogram (a), original images ((b)–(d)) and base difference ones ((e)–(h)) in AIA 193 Å. The triangles indicate the eruption locations in C. The white (black) arrows indicate the surges (loops). The box region is the same as Figure 3.

(A color version of this figure is available in the online journal.)

panels c–d). The associated EUV wave expanded outward and also dominated in the southeast (panels e–g).

Figure 6 presents the light curves in four AIA wavelengths for summed intensities in the region marked by the box in Figures 3–5. In each wavelength, there are four evident intensity enhancements, corresponding to the flares associated with the successive eruptions. Their commencements were unclear. The

flares peaked at about 18:20, 18:57, 19:45, and 20:53 UT (indicated by vertical dotted lines), respectively. The intervals between the peaks were about 37, 48, and 68 minutes, which became longer and longer.

The successive eruptions were observed at the limb in the perspective of the *STEREO-A*, but with no associated CMEs. The CMEs may be too weak to be captured by coronagraphs,
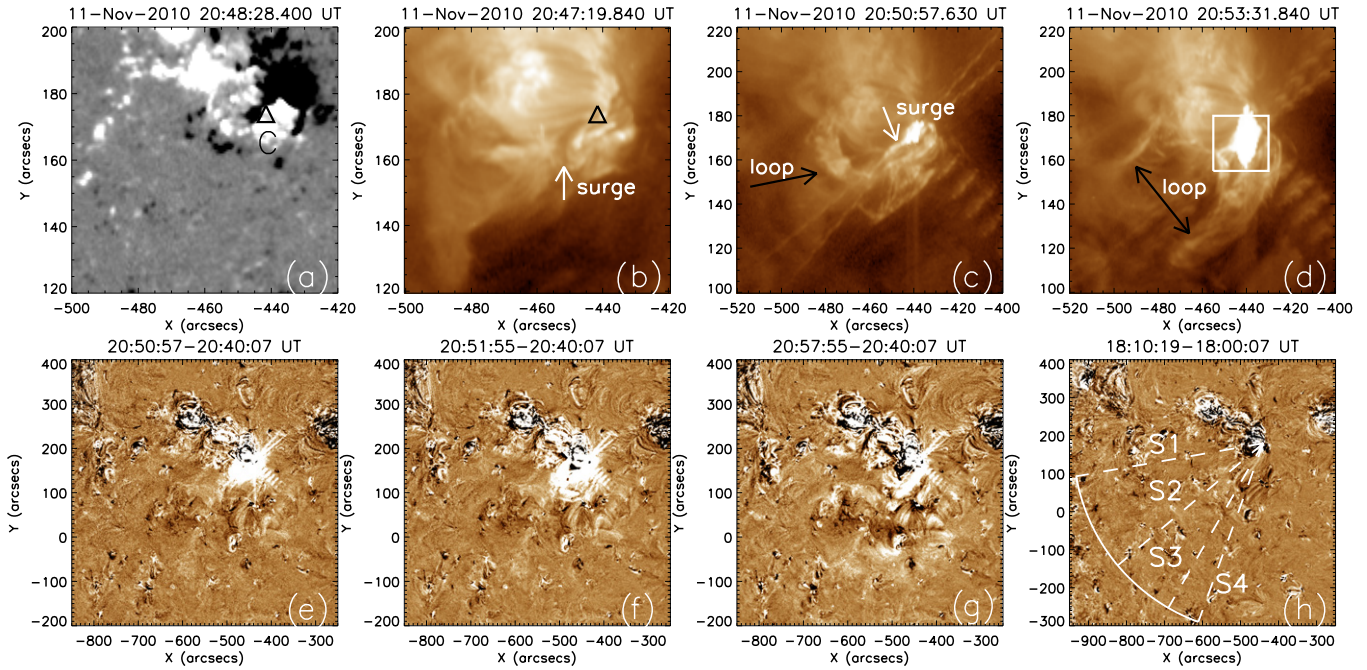
Figure 5. Evolution of E4, shown in the HMI magnetogram (a), original images (b–d), and base difference ones (e–g) in AIA 193 Å. The triangles indicate the eruption locations in C. The white (black) arrows indicate the surges (loops). The box region is the same as in Figure 3. The sectors in (h), S1–S4, are used to obtain the time-slice images in Figures 8 and 9.

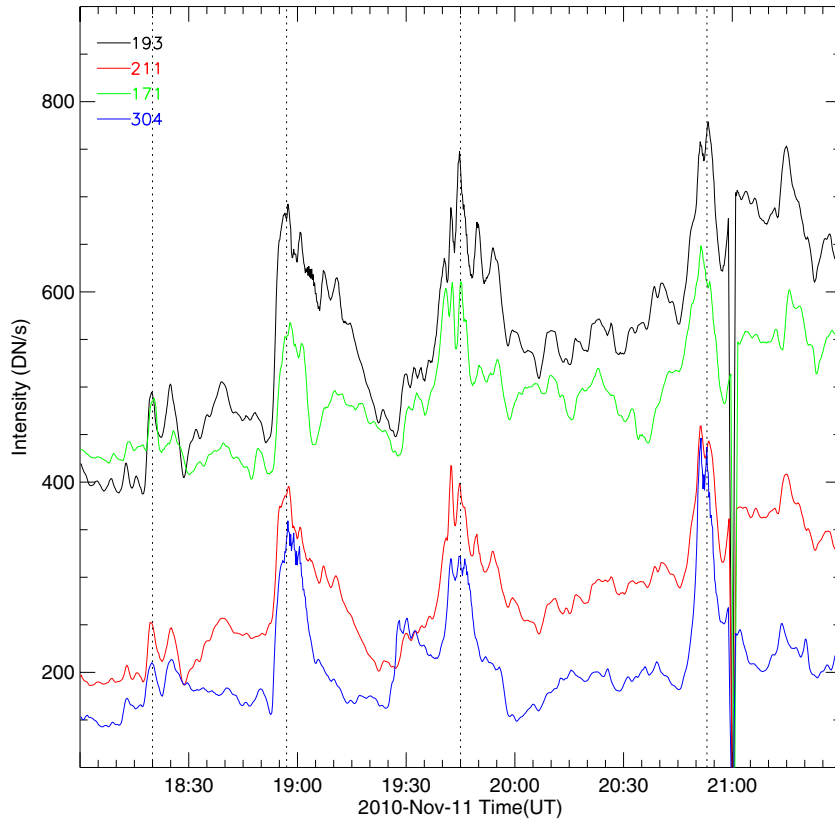(A color version of this figure is available in the online journal.)

Figure 6. Light curves of Four AIA wavelengths for summed intensities over the box region in Figures 3–5. The vertical dotted lines mark the peak times of the flares.

(A color version of this figure is available in the online journal.)

due to smaller angular extension. There were some CMEs in the period detected by the coronagraphs, but they were closely associated with the eruptions from the AR 11123 in the southern hemisphere. Figure 7 displays the evolution of the surges in base difference images of EUVI–A 304 Å (upper panels) and the expanding loops in running difference images of EUVI–A 195 Å
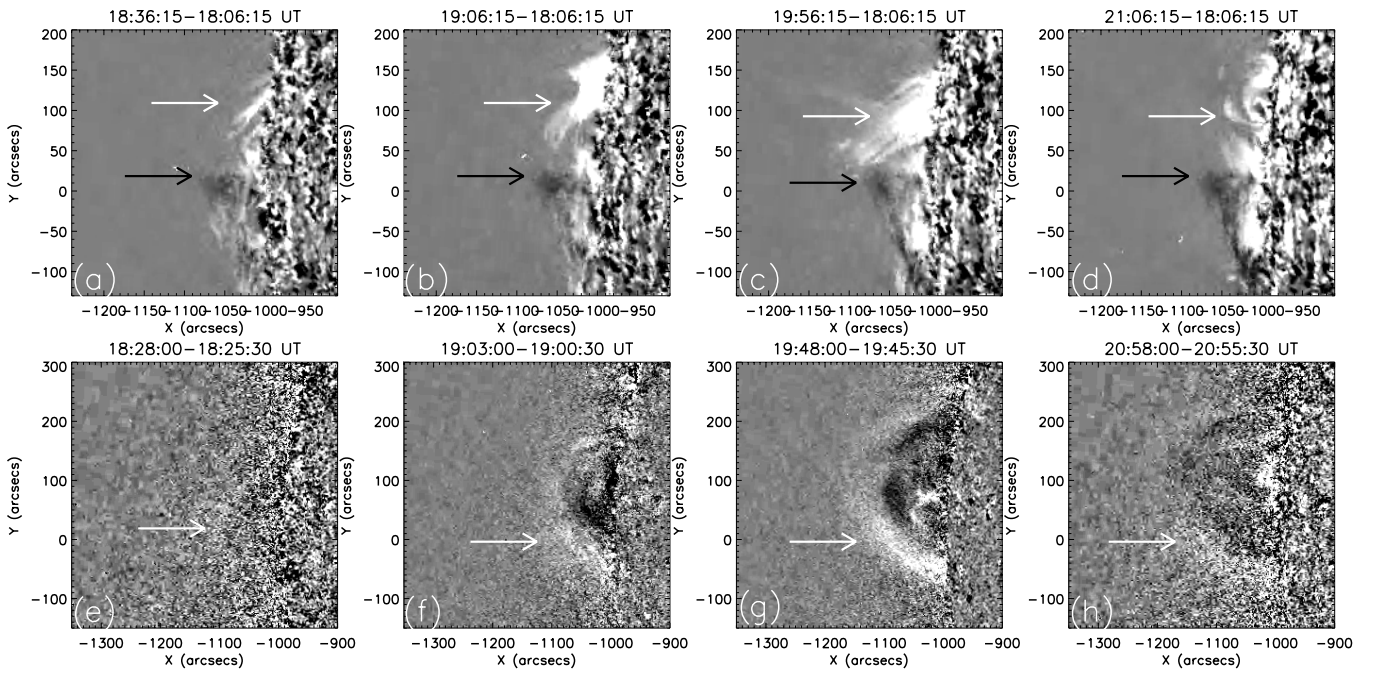
Figure 7. Base difference images in 304 Å (upper panels) and running difference images in 195 Å (bottom panels) of EUVI-A, showing the eruptive surges and the expansion loops (white arrows). The black arrows indicate the falling material of surges.

(bottom panels). Considering the timing and locations, the bright structures indicated by white arrows revealed the surges we studied, which were very distinct at the limb. The surges in E1 and E3 were straight, and those in E2 and E4 were diffuse. The dim patches were accounted for by the cooling and falling back of the surge mass (black arrows in top panels). The expanding loops in E1 were faint (the white arrow in panel e), and those in E2 and E4 were weak. The loops in E3 were bright and clear, consistent with the strongest eruptions in E3. The bright structure under the expanding loops in panel g just indicated the surge in E3. The surges and loops showed all the low corona manifestations of typical CMEs, though did not result in a proper white-light CME. It was potential that the expanding loops represented the fronts of CMEs, and the eruptive surges supplied partial mass, though most of surge material fell back.

3.3. Homologous EUV Waves and Associated Surges

In about three hours, four EUV waves emerged from the same source region with a similar appearance and propagated in the same direction, and thus we called them homologous EUV waves, referred to as W1, W2, W3, and W4 (see the animations in the online journal). To best display the EUV waves, we employ the time-slice approach and analyze the evolution of the wave fronts along the selected sectors (S1–S4) with a length of 363 Mm (500″). The angles of S1–S4 are 100°, 130°, 150°, and 160°, respectively, counted anticlockwise from the north (dashed lines in Figure 5(h)).

The left panels of Figure 6 display the propagation of the four waves in S1–S4 at 193 Å. The wave fronts appeared as bright oblique stripes of emission increase, traveling with constant velocities. The following speeds and associated errors are derived by linear fits, assuming that the measurement uncertainty of the selected points is 4 pixels (~1.74 Mm). The end points are marked as plus signs and connected by dotted lines. In S1, W1 and W2 were too faint to see. W3 was very clear, and propagated up to a distance of 250 Mm, with a velocity of about 421 ± 13 km s^{-1}. Though the front was weak,

the velocity of W4 could be detected as 415 ± 12 km s^{-1}. It is intriguing that there was a diffuse stripe with a speed of about 100 ± 3 km s^{-1}, much slower than the wave front. The diffuse stripe revealed the loop expansion in the eruption, consistent with the loop disappearance in Figure 4. Due to being far from the ejecting directions of the surges, the associated surges were not seen in S1 for all waves. In S2, long-duration deep dimmings appeared, extended to a distance of about 140 Mm. The dimmings lasted for a few hours after the event ended, resulted from the material evacuation. All the waves could be distinguished and propagated freely beyond the dimmings, although the signatures of W1, W2, and W4 were still weak. The measured velocities of W1–W4 were 312 ± 10, 308 ± 10, 419 ± 14, and 415 ± 8 km s^{-1}, respectively. Due to the influence of the dimmings, the surges were unclear. In S3, all the wave fronts were very obvious and sharp. The propagation distance for W1 was only about 150 Mm, lower than that of 250 Mm for W2 and W4. W3 was strongest and propagated up to a distance of about 360 Mm. Waves had the same velocities as those in S2, except for W3. The speed of W3 had an initial speed of 499 ± 15 km s^{-1} and decreased to 342 ± 10 km s^{-1} in the later phase. The high initial speed and deceleration may be closely related to the associated surge. The surge propagated at a high initial speed of about 253 ± 9 km s^{-1}, and faint dimmings appeared at the distance of about 180 Mm (the white arrow in panel c), which demonstrated that the mass fell back. In S4, the velocities of W1 and W2 were 289 ± 8 and 285 ± 7 km s^{-1}, respectively, slightly smaller than those in previous directions. The speed of W4 kept the same value as that in S1–S3, and the associated surge had a speed of about 167 ± 9 km s^{-1}. Similar to that in S3, W3 decreased from 499 ± 17 to 297 ± 9 km s^{-1}, and the associated surge had a speed of about 249 ± 10 km s^{-1}. The decelerating character of W3 was closely associated with the associated surge and consistent with freely propagating fast-mode waves (Veronig et al. 2008, 2010; Long et al. 2008). It is plausible that W3 was initially driven by the surge and freely propagated after the surge stopped and fell back. The associated
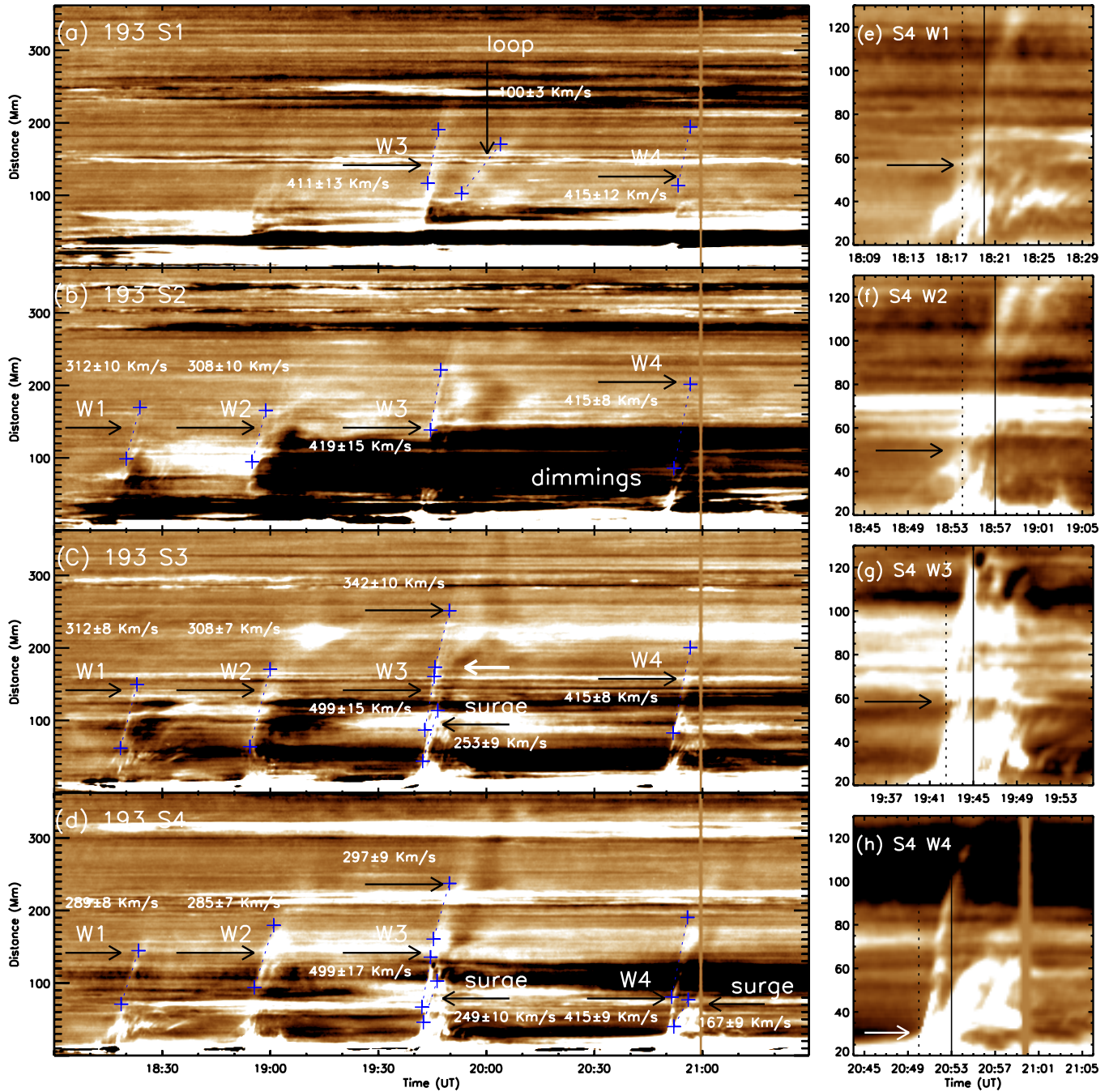
Figure 8. Base difference time-slice images along the sectors S1–S4 in AIA 193 Å (left panels) and the close-up of each wave along S4 (right panels). Wave signatures and associated surges are indicated by the arrows. Plus signs connected by dotted lines mark the selected points in linear fits, with the fitted velocities attached. The arrows in the right panels indicate the start points of waves, and the vertical solid and dotted lines represent the peak times of flares and wave commencements. The vertical strips around 21:00 UT correspond to the data gap of AIA.

(A color version of this figure is available in the online journal.)

flares and surges both started before the onsets of the waves, which was most obvious in S4. The close-ups of W1–W4 in S4 are shown in right panels. The initial locations of W1–W3 were close to the associated surges and far from the flare sites, except for W4, in which the initial location was merged in the flare site (arrows in right panels). In addition, the wave commencements (vertical dotted lines) were at about 18:18, 18:54, 19:42, and 20:50 UT, respectively, which were about three minutes before the peak times of associated flares (vertical solid lines). The intervals for waves were 36, 48, and 68 minutes, respectively. The buildup times of the magnetic energy for the next eruption were longer and longer, accordant with the results in Kienreich et al. (2011).

Next we focused on the waves in S4. The propagation of the waves in other EUV wavelengths of AIA are shown in the left panels of Figure 7. In 211 Å, waves and surges were like those in 193 Å. The velocities of the waves were 289 ± 7, 285 ± 5, 499 ± 13, and 415 ± 9 km s^{-1}, respectively, and that of W3 also decreased to about 297 ± 10 km s^{-1}. The surges in E3 and E4 were 249 ± 6 and 167 ± 8 km s^{-1}, respectively. In 171 Å, the wave fronts were replaced by the emission reduction, which suggested that the cooler material in 171 Å was probably heated
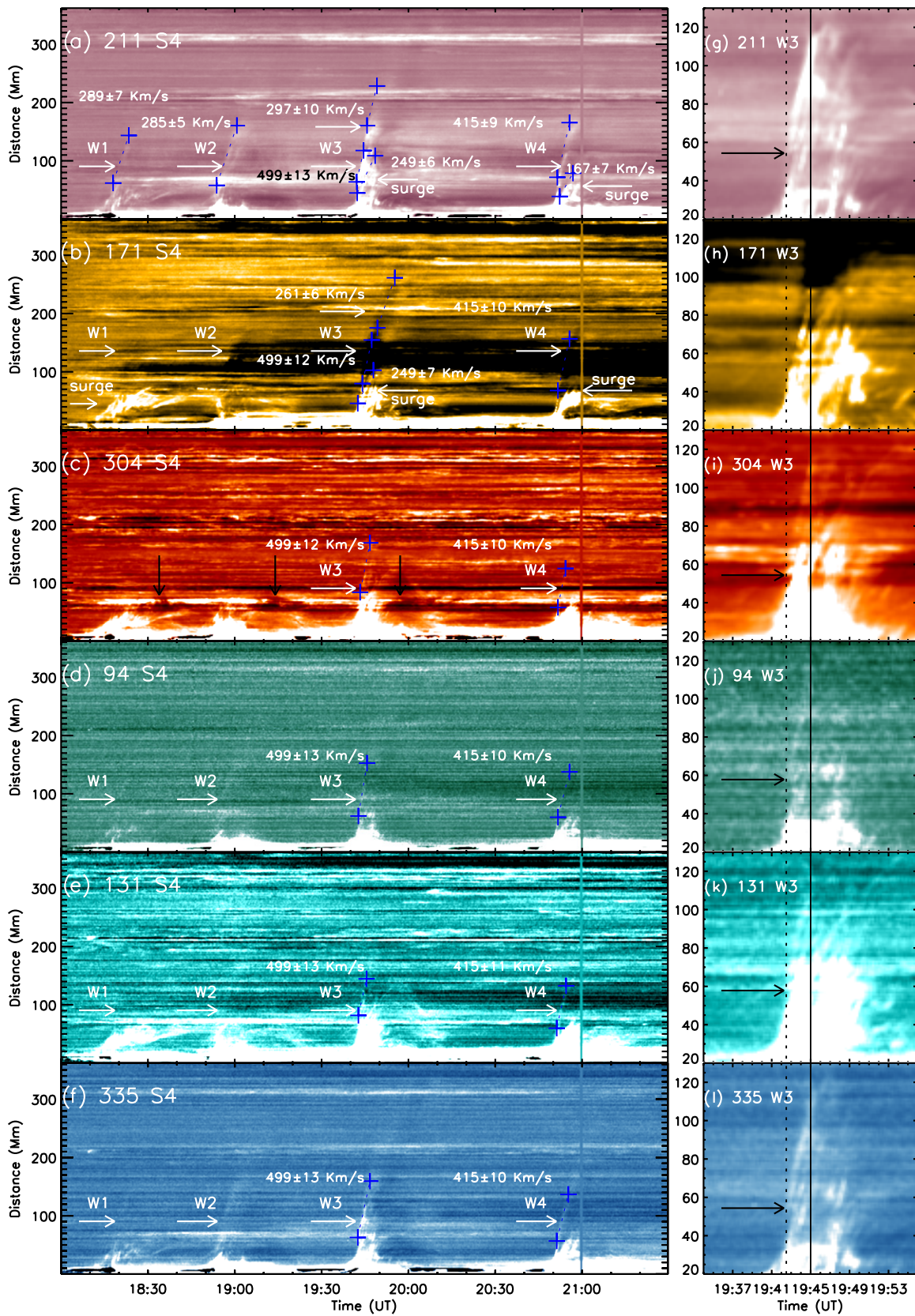
Figure 9. Base difference time-slice images along the sectors S4 in all other EUV wavelengths of AIA (left panels) and the close-up of W3 in these wavelengths (right panels). The marks are the same as those in Figure 8, except for the black arrows in panel (c), which indicate the falling material of surges.

(A color version of this figure is available in the online journal.)

to a higher temperature (Wills-Davey & Thompson 1999; Ma et al. 2009, 2011; Liu et al. 2010). W1 and W2 were faint, and the velocity of W4 was about 415 ± 10 km s^{-1}. W3 also had a high initial speed of about 499 ± 12 km s^{-1} and decreased to 261 ± 6 km s^{-1}. All the surges were obvious and bright, and the surges in E3 had a speed of about 249 ± 7 km s^{-1}. In 304 Å, the surges and their falling back were very evident (black arrows in panel (c)). The bright oblique stripes above the surges in E3 and E4 had speeds of 499 ± 12 and 415 ± 11 km s^{-1}, respectively. It was credible that they represented fronts of W3 and W4, though the deceleration of W3 was faint. In 94, 131, and 335 Å, the waves and surges had the almost same appearance. W1 and W2 were faint, and the velocity of W4 was about 415 ± 10 km s^{-1}. The initial speed of W3 was 499 ± 13 km s^{-1}, and the deceleration was also faint. In summary, W1, W2, and W4 nearly propagated at constant speeds in each AIA EUV wavelength. For W3, the high initial speed and deceleration in all of the EUV wavelengths increased the possibility that it was driven by the surge and freely propagated after the surge stopped. The close-up of W3 in these wavelengths is shown in right panels. The W3 commencement (the vertical dotted line) was about three minutes before the flare peak time (the vertical solid line). The initial location in 171 Å was too faint to be fixed because of the material heating. However, the initial locations in the other wavelengths were clearly far from the flare sites and close to the surges (arrows in the right panels), which likely indicate that the driver of W3 was closely associated with the surge.

4. DISCUSSION AND CONCLUSIONS

On 2010 November 11, four EUV waves emerged from the same source region, traveling in the same direction, and had a similar shape and angular extent. Hence, we called them homologous EUV waves. Combining the observations from AIA, HMI, and EUVI, we present a detailed study of the homologous EUV waves and their associated eruptions. Our main findings are as follows. (1) In the source region, an EFR appeared some hours before the onset of these events, and kept growing until the end of the day. The continuous emergence and cancellation of the magnetic flux was closely associated with the homologous waves and the successive eruptions. (2) The velocities of the waves were in a range of 280–500 km s^{-1}, on the order of the average surface-projected expansion speeds for fast-mode waves (Wang 2000). Each wave almost propagated at a constant velocity with very little direction dependence, which was consistent with a fast-mode MHD wave (e.g., Kienreich et al. 2009; Ma et al. 2009; Liu et al. 2010). In particular, W3 had a higher initial speed and deceleration in the ejection directions of the associated high-speed surge. It was plausible that W3 was driven by the surge and freely propagated after the surge stopped. (3) We shown the homologous waves and associated surges in all the EUV wavelengths of AIA, and they had basically the same appearance in these wavelengths in the same direction, especially for W3 and W4. The start points of W1–W3 were far from the flare sites and above the associated surges, except for W4, in which the start point was merged in the flaring region. Therefore, our results support the hypothesis that the homologous EUV waves were fast-mode waves.

The multiple homologous waves consisted of four single waves, and each one had the same characteristics as well as the single fast-mode wave. The discrepancy between multiple and single waves would be the special physical conditions in the source region, which could trigger successive single waves

in a short period. Kienreich et al. (2011) first presented four homologous EUV waves observed by the EUVI within eight hours, accompanied by weak flares and faint CMEs. They used the visual method and the profile method to derive the wave kinematics, which were analyzed in the aspects of the velocities, amplitudes, and magnetosonic Mach numbers. They regarded the homologous waves as nonlinear fast-mode waves, but did not survey the physical conditions of the source region and the wave origins. Now, we exhibit another four homologous EUV waves with the best EUV observations and photospheric data of *SDO*, in a shorter duration of three hours. The results are also suggestive of the fast-mode wave nature, and the increment for the magnetic energy buildup times is also consistent with the results in Kienreich et al. (2011). Furthermore, we study the magnetic activities of the source region to analyze their triggering mechanisms and examine their relations with the associated eruptions, especially for surges, in order to discuss their origins.

SDO supplies the high-cadence and sensitivity observations, which make the pursuit of the origin of the EUV waves possible. In S1, the loop expansion appeared to follow the W3 front, but the expansion speed was about one-fourth that of the W3. Therefore, it was ruled out for the field-line stretching model of Chen et al. (2002). Due to the lower cadence of limb observations and the absence of CMEs in white-light data from *STEREO*, we cannot make any conclusion regarding the relation between the waves and the CMEs. On the other hand, the waves could logically be driven by the CMEs because it is widely accepted that EUV waves are strongly associated with CMEs. As to the flares, their peak times are very close to the wave commencements. Though the initial location of each wave was far from the associated flare site, except for C4 whose start point was merged in the bright surge, we still cannot rule out the flare as the wave driver. Due to the close location and timing relations between the waves and associated surges, the surges could also generate an initially driven disturbance, which later continued to propagate freely after the surge stopped and fell back. In particular, W3 had a high initial speed and a slight deceleration in the ejection direction of the associated surge and was likely driven by the surge. We suggest that the homologous waves had more than one driving mechanism. Of course, the continuous emergence and cancellation of magnetic flux must be helpful for the launch of repetitive EUV waves in any driving mechanism.

How did the successive EUV waves occur only in three hours? Similar to homologous flares or CMEs, the key is the repeatable store–release–restore process of free energy (e.g., Li et al. 2010; Chandra et al. 2011). Recent numerical simulations have demonstrated that recurrent eruptions require the successive flux emergence into the corona or the continuously sheared motions in the photosphere (e.g., MacTaggart & Hood 2009; DeVore & Antiochos 2008). Within six hours before the first wave onset, the unsigned magnetic flux in the main part of the EFR increased about 4.5×10^{20} Mx, which was sufficient for the first wave onset. The continuous flux emergence lasted through all of the eruptions and could provide enough free energy for the other eruptions. In addition, the successive magnetic cancellation occurred around PILs and increased the stress of the coronal magnetic field, which would benefit the eruption initiation. To sum up, it is highly plausible that repetitive EUV waves could occur in the EFRs.

However, the weak intensity of the EUV waves and associated eruptions make their nature uncertain and leave other

possibilities open. More examples of homologous waves would be helpful for understanding their nature and the relation with associated eruptions. The nature of EUV waves remains subtle; further observations and theoretical work will be essential.

REFERENCES

Attrill, G. D. R. 2010, ApJ, 718, 494
Attrill, G. D. R., Harra, L. K., van Driel-Gesztelyi, L., & Démoulin, P. 2007, ApJ, 656, L101
Biesecker, D. A., Myers, D. C., Thompson, B. J., et al. 2002, ApJ, 569, 1009
Chandra, R., Schmieder, B., Mandrini, C. H., et al. 2011, Sol. Phys., 269, 83
Chen, P. F. 2006, ApJ, 641, L153
Chen, P. F., Fang, C., & Shibata, K. 2005, ApJ, 622, 1202
Chen, P. F., & Wu, Y. 2011, ApJ, 732, L20
Chen, P. F., Wu, S. T., Shibata, K., & Fang, C. 2002, ApJ, 572, L99
Chertok, I. M., & Grechnev, V. V. 2005, Sol. Phys., 229, 95
Cliver, E. W., Laurenza, M., Storini, M., & Thompson, B. J. 2005, ApJ, 631, 604
Cohen, O., Attrill, G. D. R., Manchester, W. B., IV, & Wills-Davey, M. J. 2009, ApJ, 705, 587
Delannée, C. 2009, A&A, 495, 571
Delannée, C., Török, T., Aulanier, G., & Hochedez, J. F. 2008, Sol. Phys., 247, 123
DeVore, C. R., & Antiochos, S. K. 2008, ApJ, 680, 740
Downs, C., Roussev, I. I., van der Holst, B., et al. 2011, ApJ, 728, 2
Gallagher, P. T., & Long, D. M. 2011, Space Sci. Rev., 158, 365
Gilbert, H. R., & Holzer, T. E. 2004, ApJ, 610, 572
Gopalswamy, N., Yashiro, S., Temmer, M., et al. 2009, ApJ, 691, L123
Howard, R. A., Moses, J. D., Vourlidas, A., et al. 2008, Space Sci. Rev., 136, 67
Kaiser, M. L., Kucera, T. A., Davila, J. M., et al. 2008, Space Sci. Rev., 136, 5
Kienreich, I. W., Temmer, M., & Veronig, A. M. 2009, ApJ, 703, L118
Kienreich, I. W., Veronig, A. M., Temmer, M., et al. 2011, ApJ, 727, L43
Klassen, A., Pohjolainen, S., & Klein, K.-L. 2003, Sol. Phys., 218, 197
Klein, K.-L., Khan, J. I., Vilmer, N., Delouis, J.-M., & Aurass, H. 1999, A&A, 346, L53
Lemen, J. R., Title, A. M., Akin, D. J., et al. 2011, Sol. Phys.
Li, Y., Lynch, B. J., Welsch, B. T., et al. 2010, Sol. Phys., 264, 149
Liu, W., Nitta, N. V., Schrijver, C. J., Title, A. M., & Tarbell, T. D. 2010, ApJ, 723, L53
Liu, W., Title, A. M., Zhao, J. W., et al. 2011, ApJ, 736, L13
Long, D. M., Gallagher, P. T., McAteer, R. T. J., & Bloomfield, D. S. 2008, ApJ, 680, L81
Ma, S. L., Raymond, J. C., Golub, L., et al. 2011, ApJ, 738, 160
Ma, S. L., Wills-Davey, M. J., Lin, J., et al. 2009, ApJ, 707, 503
MacTaggart, D., & Hood, A. W. 2009, A&A, 508, 445
Moreton, G. E. 1960, AJ, 65, 494
Moses, D., Clette, F., Delaboudinière, J.-P., et al. 1997, Sol. Phys., 175, 571
Narukage, N., Ishii, T. T., Nagata, S., et al. 2008, ApJ, 684, L45
Ofman, L., & Thompson, B. J. 2002, ApJ, 574, 440
Thompson, B. J., Gurman, J. B., Neupert, W. M., et al. 1999, ApJ, 517, L151
Thompson, B. J., & Myers, D. C. 2009, ApJS, 183, 225
Thompson, B. J., Plunkett, S. P., Gurman, J. B., et al. 1998, Geophys. Res. Lett., 25, 2465
Uchida, Y. 1968, Sol. Phys., 4, 30
Veronig, A. M., Muhr, N., Kienreich, I. W., Temmer, M., & Vršnak, B. 2010, ApJ, 716, L57
Veronig, A. M., Temmer, M., & Vršnak, B. 2008, ApJ, 681, L113
Wang, H., Shen, C., & Lin, J. 2009, ApJ, 700, 1716
Wang, J., Li, W., Denker, C., et al. 2000, ApJ, 530, 1071
Wang, Y. M. 2000, ApJ, 543, L89
Warmuth, A. 2010, Adv. Space Res., 45, 527
Wills-Davey, M. J. 2006, ApJ, 645, 757
Wills-Davey, M. J., & Attrill, G. D. R. 2009, Space Sci. Rev., 149, 325
Wills-Davey, M. J., DeForest, C. E., & Stenflo, J. O. 2007, ApJ, 664, 556
Wills-Davey, M. J., & Thompson, B. J. 1999, Sol. Phys., 190, 467
Wu, S. T., Zheng, H. N., Wang, S., et al. 2001, J. Geophys. Res., 106, 25089
Zheng, R. S., Jiang, Y. C., Hong, J. C., et al. 2011, ApJ, 739, L39
Zhukov, A. N., & Auchère, F. 2004, A&A, 427, 705